

Supplementary Material for

The sharp turn: Backward rupture branching during the 2023 M_w 7.8 Kahramanmaraş (Türkiye) earthquake

Xiaotian Ding¹, Shiqing Xu^{1*}, Yuqing Xie², Martijn van den Ende², Jan Premus², and Jean-Paul Ampuero²

¹Department of Earth and Space Sciences, Southern University of Science and Technology, Shenzhen, China

²Université Côte d'Azur, IRD, CNRS, Observatoire de la Côte d'Azur, Geoazur, Nice, France

*Corresponding author: Shiqing Xu (xusq3@sustech.edu.cn)

S1. Estimation of D_c based on D_c''

Figures S1-S3 show the information for estimating the critical slip-weakening distance D_c and the obtained results. We use unfiltered seismograms with baseline correction: we remove the mean value of acceleration recordings before the earthquake and a fitted quadratic function from velocity. As mentioned in the main text, D_c is not directly measured but estimated by a proxy D_c'' , defined as two times the fault-parallel displacement at the time of peak ground velocity measured at short distance from the fault (Figure S2). The proxy D_c'' is an upper bound of the value D_c' that would be measured exactly on the fault, and D_c' itself is a representative approximation of the actual D_c . We use the data retrieved from the entire portion of the EAF southwest of the junction with the initial splay fault (Figures S1 and S3), whereas in our numerical simulations we only focus on the region near the junction. Figure S3 shows our D_c'' estimates, their uncertainties and their spatial variability.

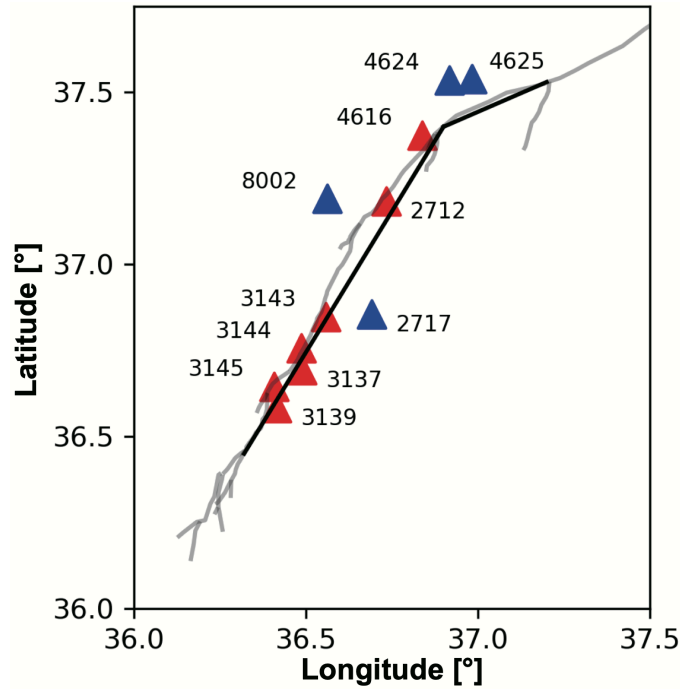


Figure S1. Location of selected stations close to the fault surface rupture. We focus on the southern portion of the EAF, SW from its junction with the initial splay fault. The grey lines show surface ruptures (Reitman et al., 2023), the black line shows the simplified geometry considered to compute along-strike positions in Figure S3, and triangles show the position of stations at a distance from the fault shorter (red) and larger (blue) than 1 km.

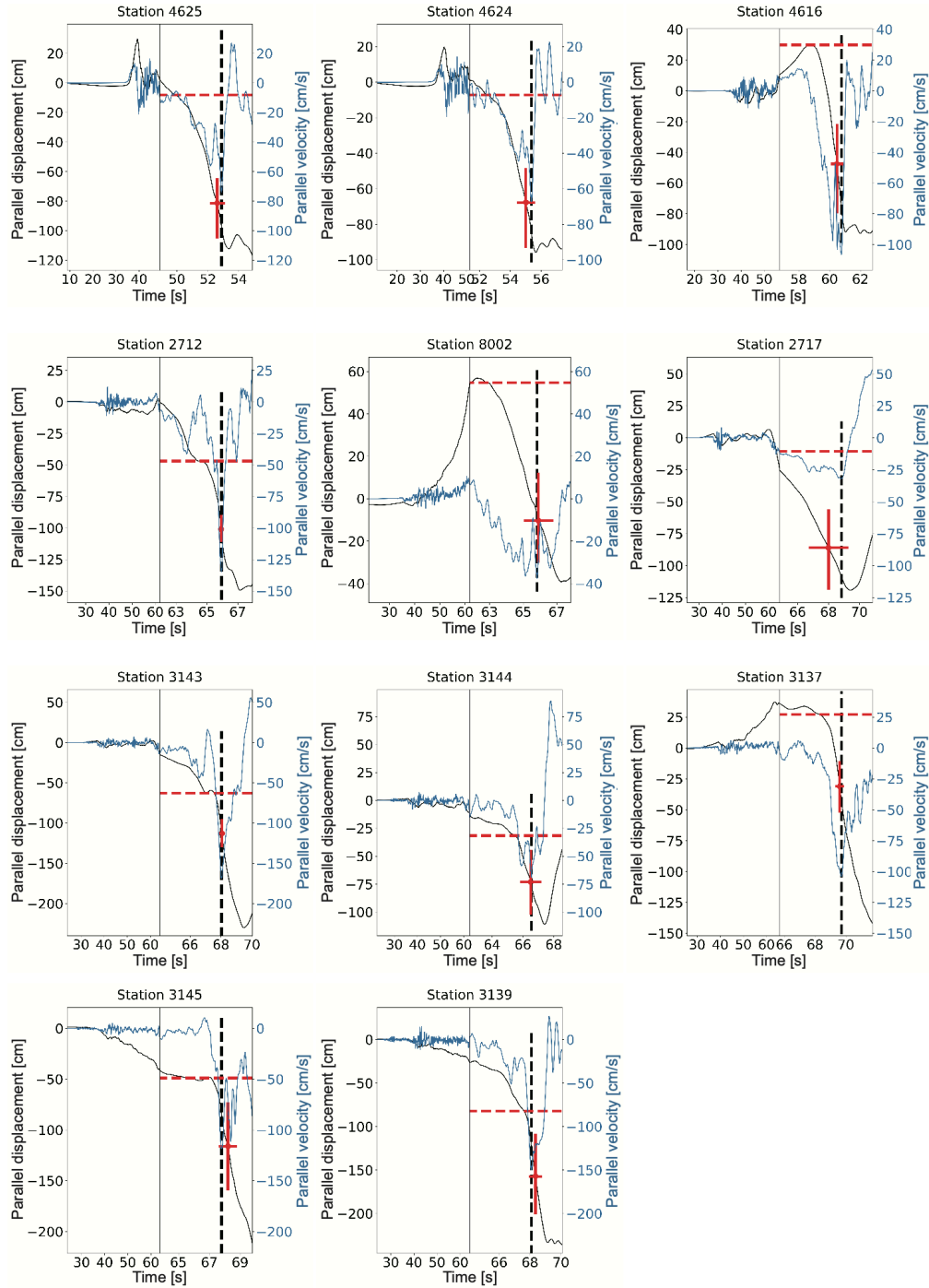


Figure S2. Fault-parallel velocity (blue) and displacement (black) obtained by integrating acceleration data with baseline correction. The horizontal red-dashed line denotes the displacement level right before the passage of the SW-ward rupture front near the station; this value is taken as the reference to estimate D_c'' . The vertical black dashed line indicates the time of maximum velocity. The red cross shows an estimate of the uncertainty of maximum velocity (horizontally) and corresponding displacement (vertically). The red dot in their intersection indicates a mean value of peak-velocity time and displacement.

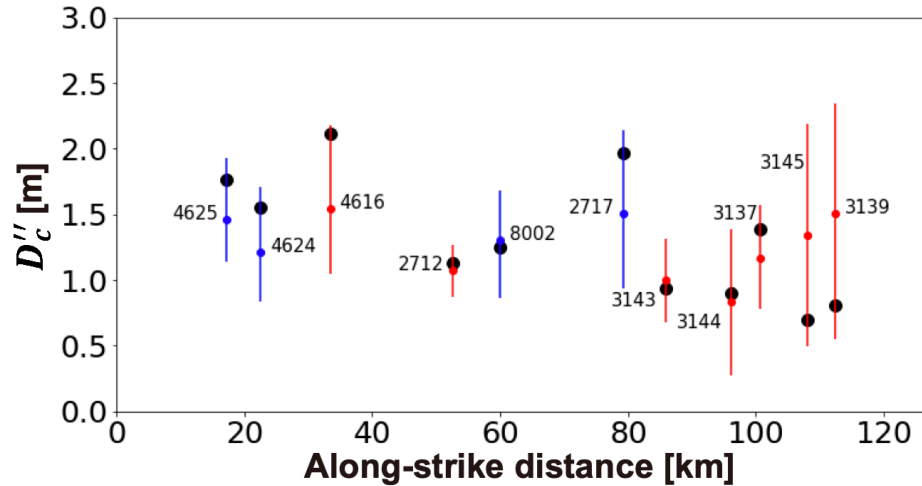


Figure S3. Along-strike distribution of estimated D_c'' . The distance in the horizontal axis is relative to the junction between the splay and main faults (see Figure S1). Large black dots show the value of D_c'' estimated from the displacement at the time of maximum velocity. Vertical bars show the D_c'' uncertainty inferred from the maximum velocity uncertainty, while small dots (in blue or red) show D_c'' at the center of the uncertainty interval. Colors indicate stations at a distance from the fault shorter (red) and larger (blue) than 1 km, as in Figure S1.

S2. Additional results for delayed rupture triggering on the SW segment of the main fault

For comparison, we first examine one case similar to that in Figure 6, but with the NE segment of the main fault effectively locked (Figure S4). Under this condition, the SW segment of the main fault is not activated, further illustrating the necessity of the NE-ward rupture for triggering the SW-ward rupture along the main fault. In addition to the subshear case shown in the main text (Figures 5 and 6), we also report a case of supershear rupture along the splay fault, which successfully triggers first the NE segment of the main fault (Figures S5 and S6). The overall behavior of the triggered rupture along the main fault (Figure S6) is similar to that of the previous case (Figure 6). The main differences lie in the transient stress field before the splay-fault rupture is fully terminated at the junction. In the supershear case (Figure S5), the stress field comprises three parts that sequentially sweep along the SW segment of the main fault (Mello et al., 2010, 2016). The first one is carried by the dilatational field (zero curl) of the supershear front (Bhat et al., 2007) and exerts a transient positive ΔCFS (t_1 to t_2 in Figure S5a, Figure S5b and c). The second one is carried by the S-wave Mach front and exerts a transient negative ΔCFS (around t_3 in Figure S5a, Figure S5d). The third one is carried by the trailing Rayleigh wave but is too weak to observe (Figure S5d). None of these three parts triggers a rupture along the SW segment of the main fault in the case shown in Figure

S5; successful triggering along the SW segment occurs only after the NE segment is activated (Figure S5f and g), similar to the previous case shown in Figure 5.

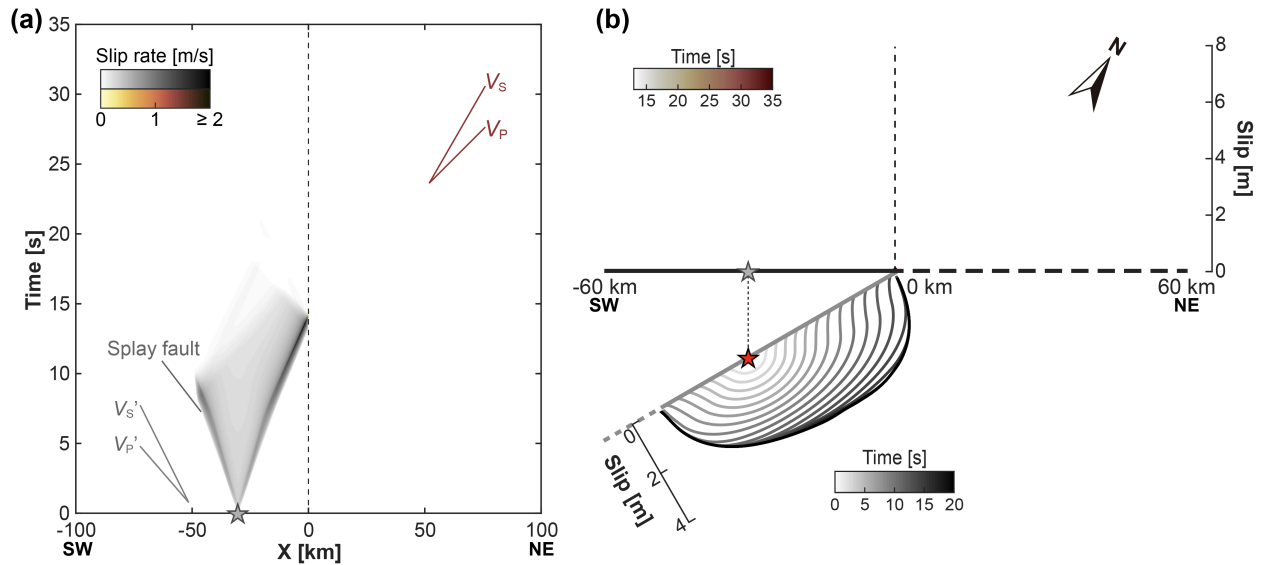


Figure S4. Similar to Figure 6 but for one case where the NE segment of the main fault is forced to remain locked under an assumed fault cohesion of 30 MPa. In this case, no rupture is triggered on the SW segment of the main fault.

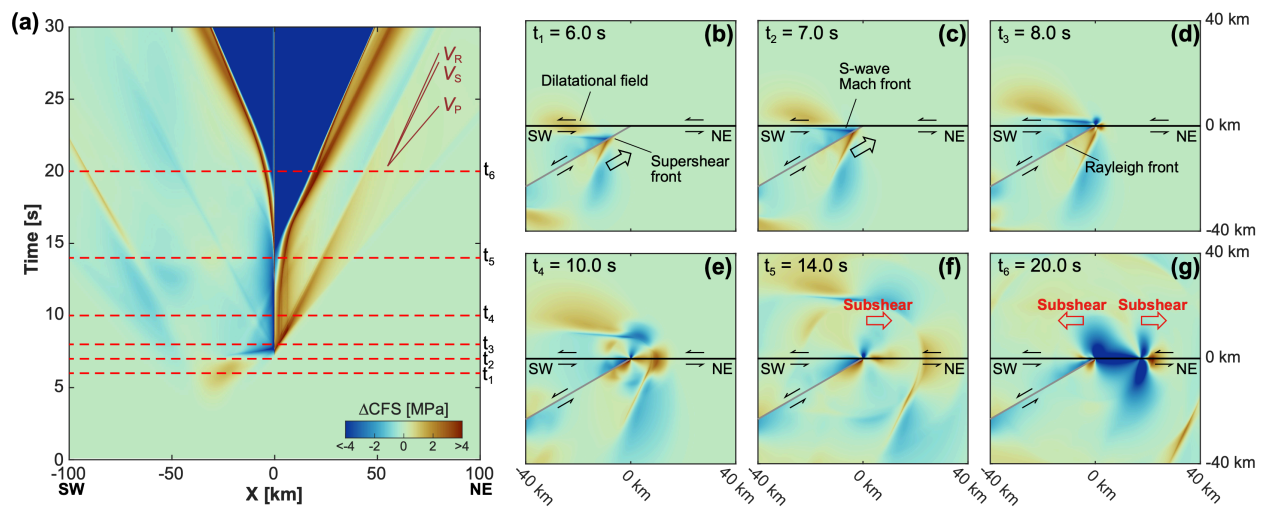


Figure S5. Spatiotemporal distribution of Coulomb failure stress change (ΔCFS) induced by a supershear rupture along the splay fault. (a) Evolution of ΔCFS projected along the main fault. Six times t_1 to t_6 are selected to highlight (1) when a dilatational stress lobe ($\Delta\text{CFS} > 0$) operates on the SW segment of the main fault, (2) when the S-wave Mach front ($\Delta\text{CFS} < 0$) is about to sweep over the SW segment next to the junction, (3) when the supershear rupture front just hits the junction along the splay fault, (4) when arrest waves start to radiate outward from the junction, (5) when rupture is just triggered along the NE segment of the main fault, (6) when the SW segment is activated by the stress transfer from the NE-ward

propagating rupture. (b)-(g) Spatial distribution of ΔCFS , resolved onto faults parallel to the main fault, at the six different times defined in (a). $f^{eff} = 0.48$ is assumed to compute ΔCFS (Eq. 3). Other model parameters are: $f_s^{sp} = 0.21$, $f_d^{sp} = 0.10$, $D_c^{sp} = 0.50$ m; $f_s^m = 0.48$, $f_d^m = 0.29$, $D_c^m = 1.00$ m. Under these conditions, the corresponding values for seismic S ratio are: $S^{sp} = 0.08$ and $S^m = 0.73$.

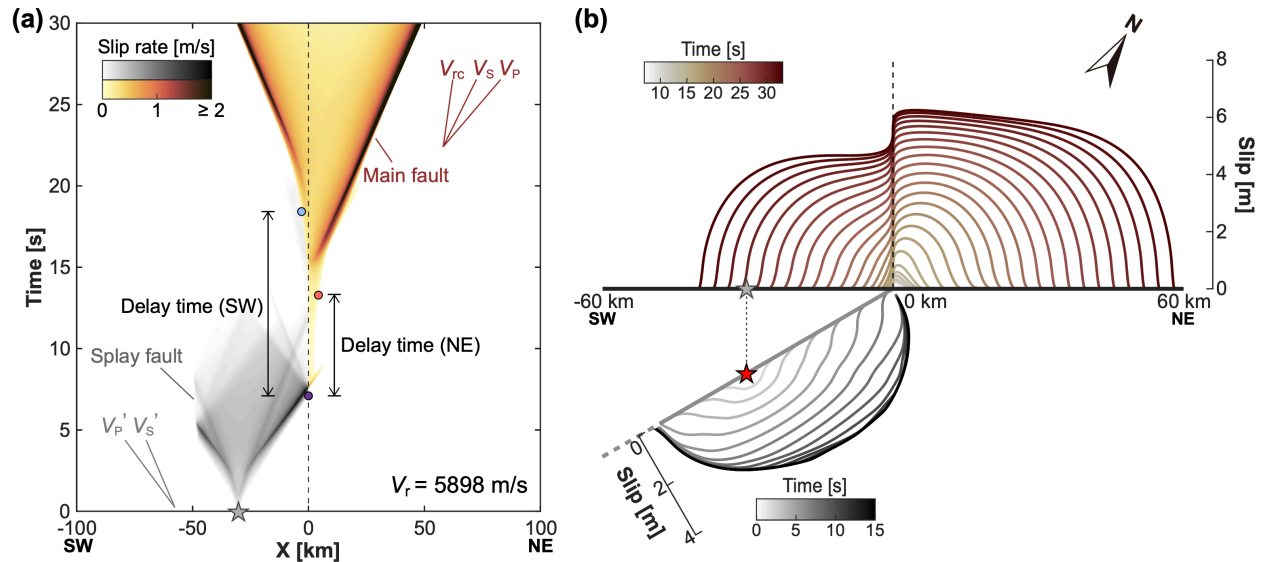


Figure S6. Spatiotemporal distribution of (a) slip rate and (b) slip for the case shown in Figure S5. In (a), V_r (5898 m/s) denotes the instantaneous propagation speed of the splay-fault rupture prior to its arrival at the junction with the main fault. The delay time is defined in the same way as in Figure 6.

S3. Additional results for early rupture triggering on the SW segment of the main fault

Here, we document the possibility of rupture triggering first on the SW segment of the main fault (Section 3.4) by reporting additional numerical simulation results. Figure S7 shows the evolution of ΔCFS for the case in Figure 11, in which a splay-fault subshear rupture triggers first the SW segment. The rupture along the SW segment is initiated around t_2 (Figure S7c) and shows bilateral propagation from t_3 to t_4 (Figure S7d and e). Additional test shows that, even with the NE segment of the main fault effectively locked, the activated rupture along the SW segment can continue its propagation (Figure S8). Earlier triggering can also be achieved by a supershear rupture along the splay fault (Figures S9 and S10). The dilatational stress carried by the splay-fault supershear front produces the earliest triggering along the SW segment (around t_2 in Figure S9). The following S-wave Mach front, though associated with a negative ΔCFS , does not stop the rupture triggered along the SW segment (t_3 to t_4 in Figure S9). Upon the arrival of the splay-fault rupture at the junction, a second rupture is triggered (after t_4 in Figure S9a), slightly skewed to the NE side of the junction along the main fault. Second rupture triggering can also be observed in the subshear

case, initiated at the junction along the main fault (Figure S7), but is somewhat overshadowed by the first rupture. We expect this second rupture to follow the same mechanism as analyzed in Section 3.2.

Finally, we report an additional set of results on the delay time along the main fault (Figure S11). Here, we focus on the SW-ward rupture triggered along the main fault, including cases triggered first on the NE segment (marker with black edge color, as in Figure 6) and first on the SW segment (marker with red edge color, as in Figure 11). We do not consider second rupture triggering, even if it contains a SW-ward component (e.g., initiated at the fault junction in Figures S9 and S10). We overall find that, to trigger first the SW segment, the main fault must be initially close to failure (extremely low values of S^m).

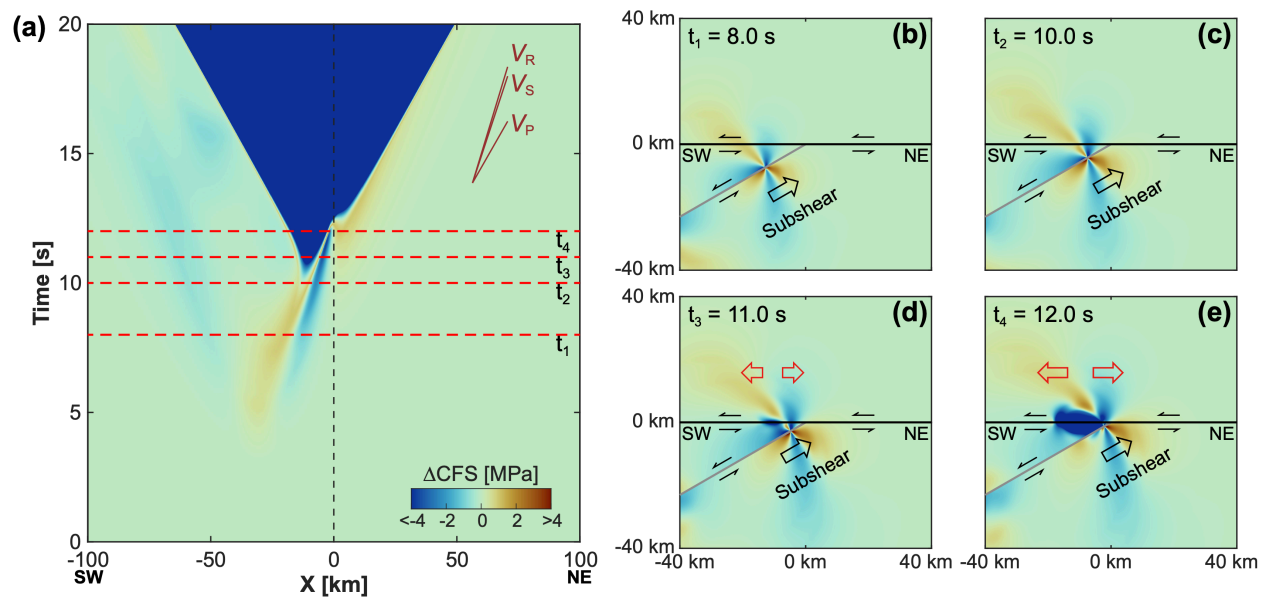


Figure S7. Similar to Figure S5 but for a subshear rupture along the splay fault that triggers rupture of the main fault first along its SW segment, before the splay-fault rupture arrives at the junction. $f^{eff} = 0.42$ is assumed to compute ΔCFS (Eq. 3). Other model parameters can be found in Figure 11, which shows the corresponding evolutions of slip rate and slip.

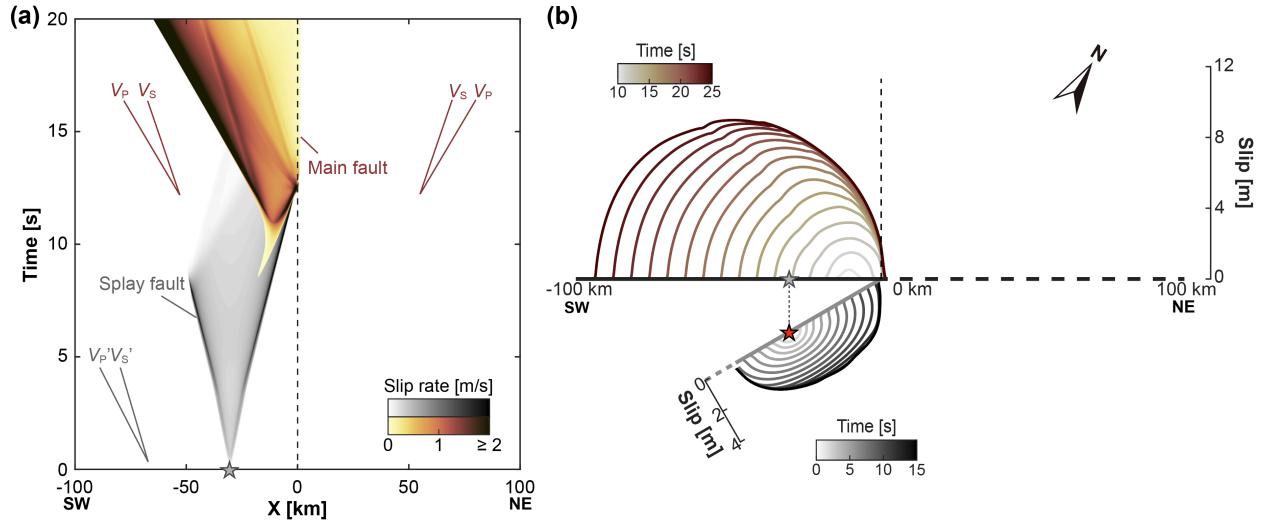


Figure S8. Similar to Figure 11 but for one case where the NE segment of the main fault is forced to remain locked under an assumed fault cohesion of 30 MPa. In this case, an early rupture is triggered on the SW segment of the main fault before the splay-fault rupture reaches the junction. Moreover, the triggered main-fault rupture can continue its propagation to the SW.

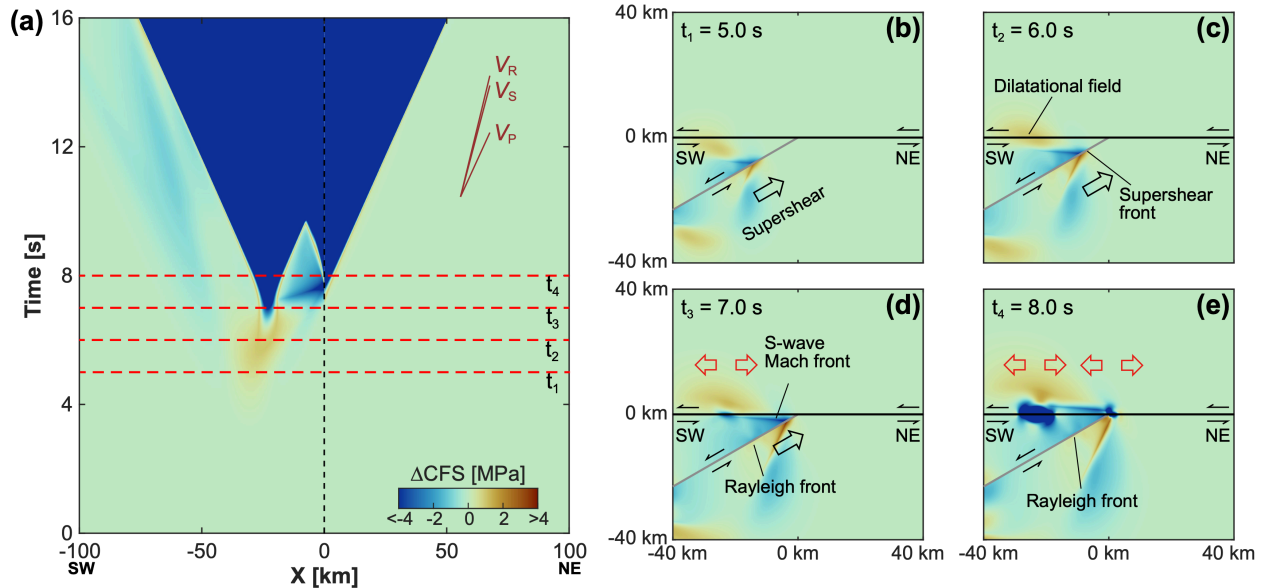


Figure S9. Similar to Figure S7 but for a supershear rupture along the splay fault. Here also, rupture of the main fault is triggered first along its SW segment, before the splay-fault rupture arrives at the junction, and $f^{eff} = 0.42$. Other model parameters are: $f_s^{sp} = 0.21$, $f_d^{sp} = 0.10$, $D_c^{sp} = 0.50$ m; $f_s^m = 0.42$, $f_d^m = 0.20$, $D_c^m = 0.50$ m. Under these conditions, the corresponding values for seismic S ratio are: $S^{sp} = 0.08$ and $S^m = 0.10$.

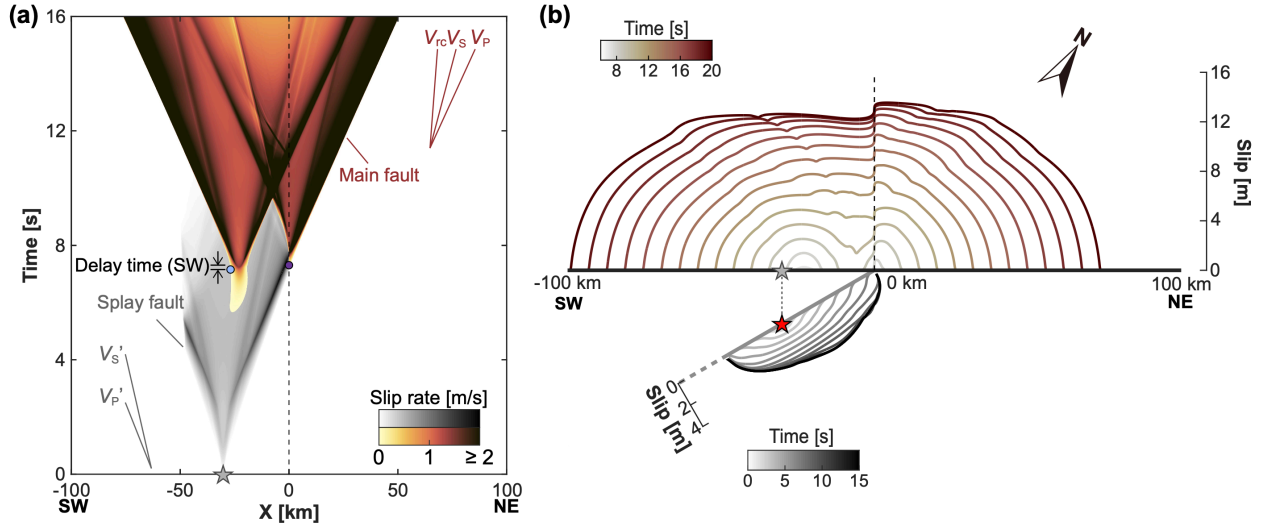


Figure S10. Spatiotemporal distribution of (a) slip rate and (b) slip for the case shown in Figure S9.

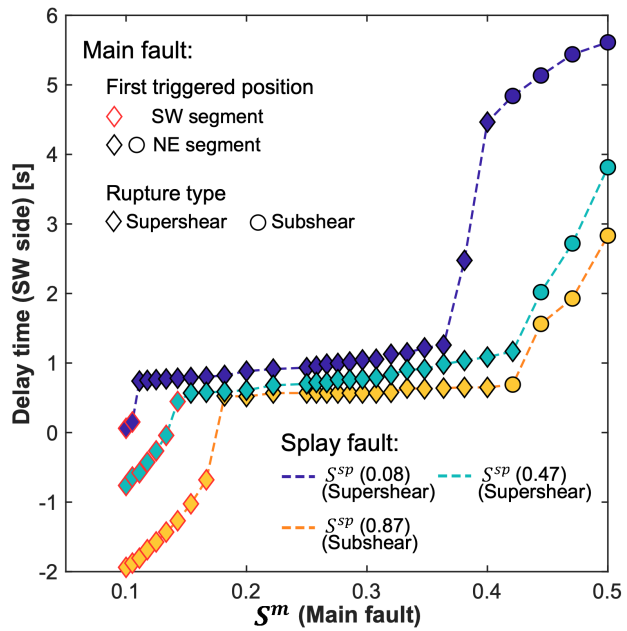


Figure S11. Delay time along the SW segment of the main fault as a function of the seismic S ratio along the main fault (S^m) and along the splay fault (S^{sp} , indicated by curve and symbol-fill-in colors). Symbols with black and red edges correspond, respectively, to the cases with triggering first along the NE segment and SW segment of the main fault. Earlier triggering on the SW segment (negative or small positive delay time) occurs only at extremely low values of S^m , i.e., when the main fault is initially very close to failure. For the main fault, we vary f_d^m (under fixed $f_s^m = 0.42$) to obtain different values of S^m . For the splay fault, we vary f_s^{sp} (under fixed $f_d^{sp} = 0.10$) to obtain different values of S^{sp} . For both the main and splay faults, D_c is fixed at 0.50 m.

References for Supplementary Material

Bhat, H. S., Dmowska, R., King, G. C., Klinger, Y., and Rice, J. R. (2007). Off-fault damage patterns due to supershear ruptures with application to the 2001 Mw 8.1 Kokoxili (Kunlun) Tibet earthquake. *Journal of Geophysical Research: Solid Earth*, 112(B6). doi: 10.1029/2006JB004425.

Mello, M., Bhat, H. S., Rosakis, A. J., and Kanamori, H. (2010). Identifying the unique ground motion signatures of supershear earthquakes: Theory and experiments. *Tectonophysics*, 493(3-4), 297–326. doi: 10.1016/j.tecto.2010.07.003.

Mello, M., Bhat, H. S., and Rosakis, A. J. (2016). Spatiotemporal properties of Sub-Rayleigh and supershear rupture velocity fields: Theory and experiments. *Journal of the Mechanics and Physics of Solids*, 93, 153–181. doi: 10.1016/j.jmps.2016.02.031.